This article has been published in Materials and Design. The final publication is available at Elsevier via https://doi.org/10.1016/j.matdes.2018.02.007

3D multi-scale multi-physics modelling of hot cracking in welding

H.R. Zareie Rajani[a], A.B. Phillion[b,*]

[a]School of Engineering, The University of British Columbia, Kelowna, BC, Canada
[b]Department of Materials Science and Engineering, McMaster University, Hamilton, ON, Canada

Abstract

A 3D multi-scale and multi-physics numerical model has been developed and validated to predict the occurrence of hot cracking during fusion welding of Al-Mg-Si alloys. The new model consists of four modules: (I) a welding solidification module that creates the desired weld microstructure consisting of both columnar and equiaxed grains and varies as a function of welding conditions; (II) a thermo-mechanical analysis module that predicts the deformation of the weld mushy zone due to solidification contraction and the response of the base metal; (III) a fluid flow module that calculates the variation in fluid velocity and pressure within the micro liquid channels of the semisolid; and (IV) a crack initiation module that applies Kou's hot cracking criterion [1] to identify cracked liquid channels based on inputs from the solidification, thermo-mechanical and fluid-flow modules. The results identify the underlying mechanisms by which welding process parameters (current and travel speed) and external restraining conditions influence hot cracking susceptibility during Gas Tungsten Arc welding. Interestingly, micro hot cracks seem to initiate near the fusion zone but then localize and form a macroscopic hot crack at the core of the weld

*Corresponding author
Email address: andre.phillion@mcmaster.ca (A.B. Phillion)

Keywords: Solidification, Welding Modelling, Multi- physics, Hot Cracking, Mesoscale

1. Highlights

A 3D multi-scale and multi-physics mathematical model has been developed and validated to simulate the fusion welding of Al-Mg-Si alloys. The metallurgical mechanisms linking welding process parameters, external restraining conditions and hot cracking are discussed. The localization of hot cracks at individual grain boundaries are predicted; interestingly micro hot cracks seem to initiate near the fusion zone.

2. Introduction

Of the different fusion welding processes, Gas Tunsten Arc Welding (GTAW) and Gas Metal Arc Welding (GMAW) are most commonly used to join metal alloys because of their affordability, mobility, and reliability [2]. However, fusion welding is not defect-free. One of the main defects that forms within the weld pool is hot cracking [3]. This defect, also known as hot tearing in metal casting processes, occurs during the final stages of solidification when the solid fraction (f_s) is close to unity. Several factors are reported to affect the formation of hot cracks in both welding and casting [4]. These include: a network of thin liquid channels surrounding the solid grains; deformation of the mushy zone that induces cracks at the solid-liquid interface; and low permeability inhibiting liquid flow through the channels to prevent refilling (also called healing) of the initiated cracks [5, 6].

Experimentally, many tests have been conducted to assess alloy and process susceptibility to hot cracking (e.g. [4, 7, 8]). However, the high temperatures and the very short lifetime of the semisolid restrict the use of experimental methods when investigating the transient phenomena involved in crack initiation. Instead, numerical methods must be used as they allow for concurrent

study of solidification [6, 9, 10], semisolid deformation [11–13], and defect formation [14, 15].

In the past few years, there has been significant interest in using a granular modelling approach to study this defect [6, 12, 13, 16–25] as this method allows for simulation of the most-relevant physics within a large [1] and sometimes non-isothermal mushy zone. Unlike macro-scale simulations that model transport phenomena during welding (e.g. [26]) and casting (e.g. [27]) based on averaged equations, granular methods are able to simulate the interactions between the solid and liquid phases at the scale of the microstructure while at the same time taking into account long-range stresses and strains. Granular methods are also able to provide all of the inputs for hot cracking criteria (e.g. [1]) at the scale of the microstructure, along with spatial variations in these parameters. Combined, this allows for investigation of localization of hot cracking at grain boundaries taking into account both stochastic variations in grain morphology, and process parameters.

In granular models of semi-solids, the microstructure is approximated by a set of polyhedrons based on the Voronoi diagram of a random set of nuclei, resulting in irregular grain arrangements. Solidification is then simulated by advancing the grain edges towards the final grain boundaries along a linear segment connecting the nuclei with a Voronoi vertex. At a specified f_s, flow and deformation are simulated through the liquid channels and within the grains, respectively. Vernede et al. [20, 21] used this modelling technique to simulate, in 2D, the solidification sequence, grain percolation, and fluid flow of an Al-Cu binary alloy. Phillion et al. [17] extended Vernede's approach to 3D, showing that the third dimension allows for concurrent continuity of both the liquid and solid phase. Sistaninia et al. [6, 12, 18, 19] then developed a sophisticated 3D hydro-mechanical model to simulate the semisolid constitutive behaviour of metallic alloys. Following reconstruction of the semisolid microstructure composed of a network of micro liquid channels and solid grains, the separation of

[1] On the order of 1000s of grains

the liquid channels as a result of semisolid deformation and fluid flow was predicted. The calculated pressure and fluid velocity inside each channel were then used in conjunction with a cracking criteria to directly model hot crack initiation and growth. Phillion et al. [16] and Zaragoci et al. [22] have also developed granular-type models to investigate additional aspects of semisolid deformation and crystal rearrangement.

Despite many similarities between casting and fusion welding processes, fundamental differences do not allow for direct use of prior granular models to investigate hot cracking in welding. First, the prior models are intended to develop equiaxed-globular microstructure and cannot reconstruct the columnar grains that form an essential part of welding microstructure. Second, semisolid deformation occurs during welding as a result of a complex and evolving thermo-mechanical stress field. Third, the weld mushy zone contains large thermal gradients and consequently large spatial variations in f_s. Ploshikhin et al. [28] introduced a preliminary integrated mechanical-metallurgical model for hot cracking during welding, examining strain accumulation in the liquid at the centerline of a laser weld using the finite element method. In this previous work, the liquid weld was modelled as a weak solid, which then interacted with the surrounding base metal. Recently, Zareie Rajani and Phillion have presented a set of numerical modules as initial steps towards developing a comprehensive 3D multi-scale and multi-physics model of hot cracking in welding. In the first contribution, the evolving 3D semisolid weld microstructure consisting of both equiaxed and columnar grains was simulated within a granular context [29] as a function of GTAW current and travel speed. In the second contribution, the transient thermo-mechanical stresses acting on the weld mushy zone were simulated to directly quantify the separation rate of the micro liquid channels [30].

Although the previous multi-scale and multi-physics models of welding solidification and semisolid deformation have provided fundamental insight into hot crack formation, they do not directly predict damage initiation that eventually leads to a hot crack. In this study, a comprehensive 3D model is proposed that couples the deformation within the weld mushy zone, fluid flow through

the micro liquid channels existing at high f_s, and hot crack initiation. This has been achieved through development of a sequential method that links the interactions between the solidification shrinkage, thermo-mechanical forces, restraining forces, and the transient pressure within the melt pool. The simulation results are applied to GTAW of AA6061 and then compared with experimental studies to assess the performance of the model.

3. Model Development

The comprehensive multi-physics and multi-scale model of hot cracking during welding is described below. It consists of four modules: a welding solidification module (WSM), a thermo-mechanical analysis module (TMM), a fluid-flow module (FFM) and a crack initiation module (CIM). The WSM creates the desired weld mushy zone microstructure for a given average f_s. This is then used by both the TMM and the FFM as the input semisolid geometry for simulating deformation and fluid flow. Physical quantities from all three modules are combined within the CIM to predict crack initiation in welding micro liquid channels.

3.1. Welding Solidification Module

The solid-liquid geometry is created using a 3-D granular model for welding. The model simulates the evolution of the weld mushy zone composed of both continuous liquid films and solidifying grains. This is accomplished by coupling a modified Voronoi tessellation to provide grain structure, the variation of f_s with temperature based on Scheil-type solidification, and imposed thermal fields calculated using the Rosenthal equation. The model is sensitive to welding conditions, creating different microstructures based on the input welding parameters by varying the number and position of the grain nuclei that define the Voronoi diagram.

The specifics are as follows (more details can be found in [29]). First, an unstructured mesh representing the as-solidified weld microstructure is generated using individual Voronoi diagrams to create the base metal, columnar zone,

and equiaxed zone, with each Voronoi cell/polyhedron denoting one grain. The nodes and elements of these diagrams are combined together to create a single continuous mesh. Second, each grain is further divided into small tetrahedral elements having one vertex at the grain nuclei and the other three on the grain surface. Third, 1D solidification is simulated within an element given a specified f_s versus temperature curve and imposed temperature evolution. The temperature at any position in any element is calculated via linear interpolation of the four nodal temperatures. At the end of solidification, the solid-liquid interfaces from opposing grains come into contact with each other and coalesce following the thermodynamic criterion proposed by Mathier [23].

The temperature field is calculated from the 3D Rosenthal equation,

$$\frac{2\pi(T-T_0)KR}{Q} = exp\left[\frac{-V(R-X)}{2\alpha}\right], \tag{1}$$

where R is the radial distance from the weld centre, X is the distance from the weld centre along the weld line, T_o is the initial temperature of the workpiece, V is the travel speed of the torch, Q is the heat transferred from the torch to the metal, and K and α are the thermal conductivity and diffusivity of the base metal. The value of Q is used as a fitting parameter to match the predictions made by the Rosenthal equation to thermocouple data from welding experiments, with each experiment having a different Q value.

The output of the WSM is a 3D representative volume element (RVE) consisting of solid grains and micro liquid channels that characterizes the microstructure within a region of the mushy zone formed during GTAW at a given average f_s. An example microstructure near the end of solidification and showing the grains and liquid channels is given in Fig. 1. Only one side of the weld is modelled due to symmetry. Due to the strong thermal gradients inherent in the process, the local f_s will vary considerably from the average value. The size of the RVE is given by the welding experimental data, which specify the weld half-width and penetration depth for each set of welding parameters. The dimension along the weld line is set to 1000 μm. This value was chosen as a compromise between capturing the entire mushy zone and computational cost.

3.2. Thermo-Mechanical Analysis Module

Semisolid deformation during welding occurs mainly as a result of solidification shrinkage and externally-applied mechanical deformation. Assuming that the walls of the micro liquid channels within the RVE remain parallel during welding [6], the deformation rate $\dot{\delta}_z^i$ of each channel can be decomposed into an internal component $\dot{\delta}_{z,int}^i$ and an external component $\dot{\delta}_{z,ext}^i$,

$$\dot{\delta}_z^i = \dot{\delta}_{z,int}^i + \dot{\delta}_{z,ext}^i. \tag{2}$$

where i is a counter representing the channel number (or more generally the element number) and z is a local coordinate having a direction perpendicular to the solid-liquid interface. The internal component represents solidification shrinkage. The external component can be further decomposed into contributions from thermo-mechanical deformation between the base metal and the weld, and the restraining forces acting along the edge of the workpiece. The output of the TMM are the $\dot{\delta}_z^i$ values for each channel. As can be seen through Eq. (2), each channel will be subject to a different deformation rate.

The internal deformation rate resulting from solidification shrinkage is given by βv^* where v^* is the velocity, $\beta = (\rho_s/\rho_l - 1)$ is the shrinkage factor, and ρ_ℓ and ρ_s are the densities of the liquid and solid. Due to the strong thermal gradients, the liquid channel walls can have different velocities especially at the columnar/equiaxed interface. Thus the general form must be decomposed into

$$\dot{\delta}_{z,int}^i = \beta(v_1^* + v_2^*), \tag{3}$$

where v_1^* and v_2^* represent the velocities of the two channel walls resulting from solidification shrinkage and given by the WSM for each micro liquid channel.

The external deformation rate is a result of solidification shrinkage in combination with mechanical deformation of the base metal. Recently, Zareie Rajani and Phillion [30] modelled the evolution of thermo-mechanical stresses that act laterally on the fusion surface to deform the mushy zone during GTAW for a given set of welding parameters at high f_s. As described in [30], these stresses can be coupled with an appropriate visco-plastic constitutive equation in order

to calculate the thermal strain rate perpendicular to the weld line, $\dot{\epsilon}_{th}$. Similarly, the restraining forces will result in an imposed strain rate applied to the edge of the work-piece also in a direction perpendicular to the weld line, $\dot{\epsilon}_{re}$. In the case of self-restraint, such as when the work-piece is clamped, $\dot{\epsilon}_{re} = 0$. The external strain rate $\dot{\epsilon} = \dot{\epsilon}_{th} + \dot{\epsilon}_{re}$ is then translated into an external deformation rate as

$$\dot{\chi}_{ext} = \dot{\epsilon} \cdot l, \tag{4}$$

where l is the initial lateral length of the mushy zone. The value of l varies with position due to the shape of the weld pool and thus the mushy zone must be discretized into a series of lateral bar elements as shown in Fig. 2 with each having a unique length l^j resulting in a unique $\dot{\chi}^j$, where j is a counter representing the bar number. Following a partitioning technique proposed by Coniglio and Cross [31], $\dot{\chi}^j$ is distributed equally among every micro liquid channel within a bar element that has a local f_s below the solid fraction for grain coalescence, f_s^{coh}. In elements having $f_s > f_s^{coh}$, it is assumed that the dendrite arms on the walls of the micro liquid channels have merged to form a solid bridge that is much stronger than unbridged channels and thus do not preferentially deform. Thus,

$$\dot{\delta}^k_{ext} = \eta \frac{\dot{\chi}^j}{N_u^j}, \tag{5}$$

where N_u^j is the number of unbridged channels within the bar element j, k is a subset of i that identifies all the micro liquid channels within the bar element j, and η has a value of 0 if f_s is greater than f_s^{coh} and 1 otherwise. Finally, as the micro liquid channels have random orientations within the mushy zone whereas the term $\dot{\chi}_{ext}$ acts lateral to the fusion surface, Eq. (5) is further modified to yield the component of $\dot{\delta}^k_{ext}$ along the local z direction of the micro liquid channel k,

$$\dot{\delta}^k_{z,ext} = \eta \frac{\dot{\chi}^j (\vec{e}_Y \cdot \vec{e}_z{}^k)}{N_u^j}, \tag{6}$$

where $\vec{e}_Y$ and $\vec{e}_z$ represent unit vectors in the global Y direction and the local z direction for channel k.

3.3. Fluid Flow Module

The solidification shrinkage as well as the externally-applied deformations, both calculated within the TMM on individual channels, act as a driving force to induce fluid flow in the weld mushy zone. Flow occurs from the weld pool into the network of micro liquid channels. The FFM then calculates the variation in fluid velocity and pressure on all the micro liquid channels within the domain. The FFM is based on Sistaninia et al. [6] granular fluid flow model, uses the unstructured mesh from the WSM to describe the geometry of the micro liquid channels, assumes that flow occurs only within the interconnected intergranular regions (i.e. not through interdendritic regions within grains) and parallel to the walls of each micro liquid channel, and is laminar, incompressible and irrotational.

The Navier-Stokes equation with the above assumptions leads to the Poiseuille flow equation between two parallel plates [6],

$$\vec{v}_\ell = \frac{1}{2\mu_\ell}\vec{\nabla} p_\ell [z^2 - h^2], \tag{7}$$

where $\vec{v}_\ell$ is the fluid velocity parallel to the walls of the micro liquid channel having x and y components, p_ℓ is the pressure in the liquid, μ_ℓ is the dynamic viscosity, and h is the half-width of the micro-liquid channel. By combining Eq. (7) with a local mass balance taking into account channel deformation resulting from Eq. (2), the pressure in a micro liquid channel is given by

$$\frac{2h^3}{3\mu_\ell}\nabla^2 p_\ell = \dot{\delta}_z^k, \tag{8}$$

$$i.e.\ \frac{2h^3}{3\mu_\ell}\nabla^2 p_\ell = \dot{\delta}_{z,int}^k + \dot{\delta}_{z,ext}^k. \tag{9}$$

The left hand side of Eq. (9) provides the pressure gradient required to compensate the solidification shrinkage, thermo-mechanical deformations and restraining forces can be seen on the right hand side. Further, Eq. (9) implies that the thickness of the micro liquid channel, itself a function of the local f_s, will significantly affect the local pressure and fluid velocity. The term relating to

the restraining forces, $\dot{\delta}^k_{z,ext}$ was added in this work to Sistaninia's FFM model due to its importance on fluid flow during welding.

The FFM boundary conditions require careful consideration to ensure their applicability to GTAW. As Fig. 3(a) illustrates, solving Eq. (9) over the RVE given by the WSM requires knowledge of boundary conditions on the following surfaces: S1 inlet surface through which the molten material enters the RVE, S2 outlet surface through which the liquid leaves the RVE, S3 a top surface representing the weld/atmosphere boundary, S4 a fusion surface separating the weld mushy zone from the base metal, and S5 a symmetry plane at the centre of the weld. The specifics are as follows. S3 and S4 are set to $\vec{v} = 0$ since the molten metal cannot flow into the solid, nor escape into the atmosphere. S5 is homogeneous with $\frac{\partial p}{\partial n} = 0$. The inlet and outlet boundary conditions are more complex. Since the RVE can be located anywhere within the mushy zone, the boundary fluid velocity and boundary pressure values on the inlet and outlet are, in general, also unknown. However, if the RVE is located right behind the weld pool, the boundary pressure on the inlet surface equals the static pressure inside the weld pool, and this static pressure can be assumed to be the same as the arc pressure that acts on top of the weld pool. Similarly, if the RVE is located at the end of the mushy zone where the average f_s approaches unity, it can be assumed that $\vec{v} = 0$ since liquid cannot flow into the fully solidified weld.

The above discussion implies that the fluid flow module can only be applied to a model containing the entire weld mushy zone, from the weld pool to the fully solidified weld. This would significantly increase computation time. To overcome this limitation, the entire mushy zone is sub-divided into five smaller RVEs having continuity in average f_s at the interface between each RVE. The fluid flow and pressure in each RVE are then determined in a sequential manner as first proposed in [6] and shown schematically in Fig. 3(b). In the first step, the analysis of fluid flow begins by solving Eq. (9) in a small RVE that is in contact with the solid weld. Since there is no flux possible at the interface with fully solid material, the outlet boundary condition becomes $\vec{v} = 0$. Since fluid flow is a function of pressure gradient and not the actual pressure, the inlet

boundary condition is an imposed pressure set equal to zero. The inlet flow into the small RVE is then calculated. This value is then imposed on the outlet side of the next RVE (i.e. $q_{1,2}$ in Fig. 3(b)) and the inlet pressure set equal to zero, to again calculate the inlet flow. The process is continued for each small RVE. In the last RVE, in contact with the weld pool, the imposed pressure on the inlet side is set to the arc pressure instead of being set equal to zero. In the second step, the analysis is reversed, beginning with the RVE in contact with the weld pool. Here, the fluid velocity obtained in the last small RVE of the first step is applied as the boundary condition at the outlet, while the imposed pressure on the inlet side is set to the weld arc pressure [32]. The pressure drop across the RVE is then calculated. This process is continued until the pressure drop across the entire weld mushy zone is determined. For these simulations, the arc pressure was assumed to be 3 atm. This value was chosen based on measurements of the average stagnation pressure on the free surface of the weld pool made during the welding experiments reported in [29].

3.4. Crack Initiation Module

The crack initiation module applies Kou's micro-scale hot cracking criterion [1] to simulate the occurrence of hot cracks during welding. According to Kou's criterion, a micro liquid channel located between two solidifying grains will crack (i.e. form a void) if the separation rate of the channel walls exceeds the sum of the wall growth rate and the local feeding rate. The criterion is expressed as,

$$KCC = \frac{d\epsilon_\ell}{dt} - (1-\beta)^m \frac{df_s^m}{dt} + ((1-(1-\beta)^m f_s^m)\frac{dv_\eta}{d\eta}, \tag{10}$$

where KCC is a numeric value representing the Kou cracking index, $\frac{d\epsilon_\ell}{dt}$ is the local strain rate perpendicular to the flow direction caused by the solidification shrinkage and external strains, m is a microstructure parameter with value of 0.5 and 0.333 for columnar and equiaxed grains respectively, and the term $\frac{dv_\eta}{d\eta}$ represents the first derivative of the intergranular liquid flow velocity along the

dominant flow direction, η. If $KCC > 0$, micro liquid channels are susceptible to cracking.

The CIM uses inputs from the WSM, TMM and FFM to evaluate Kou's criterion and thus to identify micro liquid channels that have cracked as a function of average f_s. Specifically, f_s^i, and $\frac{df_s^i}{dt}$, are given by the WSM, $\frac{d\epsilon_\ell^i}{dt} = \frac{\dot{\delta}_z^i}{h}$ is given by the TMM, and the local fluid velocity vector is given by the FFM to obtain $\frac{dv_\eta^i}{d\eta}$. The method to determine this last term requires further explanation. As Fig. 4 shows, the FFM does not yield a single flow direction within a micro liquid channel but rather a fluid flux $\vec{q}$ and thus a fluid velocity vector, $\vec{v}_\ell$ at each edge. To determine the dominant flow direction, the arithmetic mean is taken from the components of each edge as

$$v_\eta^{i,x} = \frac{\sum_{ii=1}^{3} v_x^{ii}}{3} \text{ and } v_\eta^{i,y} = \frac{\sum_{ii=1}^{3} v_y^{ii}}{3}, \tag{11}$$

where $v_\eta^{i,x}$ and $v_\eta^{i,y}$ are the velocity components in x and y along the dominant flow direction in each channel i. The summation range is 1...3 because each micro liquid channel is prismatic/triangular with fluid entering along the three "sides" of the prism. This flow direction is then used to identify the dominant flow line within the element. The edges that intersect the flow line represent the inlet and outlet edges, respectively. Since the triangular elements in this model are very small, the derivative of the fluid velocity along the dominant flow direction can be obtained by,

$$\frac{dv_\eta}{d\eta} = \frac{|\vec{v}^{outlet}| - |\vec{v}^{inlet}|}{L_{flowline}}. \tag{12}$$

3.5. Model Implementation

Hot cracking during aluminum alloy welding is assessed as follows. First, the WSM, a purpose-written C++ code that uses the Voro++ open-source library to create a modified Voronoi tessellation, is executed to create welding microstructure / numerical mesh at a specified average f_s for a given set of welding parameters. Second, the TMM, a purpose-written C++ code that interfaces with the Abaqus FEA suite, is used to determine the mechanical response of

the weld mushy zone for a given welding parameters (i.e. the $\dot{\delta}^i_{z,int}$ and $\dot{\delta}^i_{z,ext}$ values for each micro liquid channel). Specifically, this is determined by (i) applying Eq. 3 using the v_1^* and v_2^* values from the WSM in order to calculate the internal deformation rates for each micro liquid channel; (ii) performing a mechanical simulation [30] on the base metal to determine the lateral stress acting on the fusion surface; and (iii) applying Eqs. 4-6 to determine the corresponding external deformation rates resulting from the lateral stresses and partition to each micro liquid liquid channel. Then, with the $\dot{\delta}^i_{z,int}$ and $\dot{\delta}^i_{z,ext}$ values, the pressure p_ℓ and the fluid velocity $\vec{v}_\ell$ are calculated using a modified version of Sistaninia's C++ FFM code [6] using the numerical mesh from the WSM. Combined, the WSM, TMM, and FFM provide all the variables/inputs required to apply Kou's criterion. Finally, the CIM is then applied to identify all the micro liquid channels that have cracked. Although not simulated in this research, the newly-formed micro cracks would join together with additional deformation to form a visible hot crack. Note that the coupling is one way only, i.e. the failed channels identified within the CIM do not influence the FFM, nor the TMM. Note also that the model is not transient but instead assesses the state of hot crack formation for a specified average f_s. Individual simulations are then performed for different values of f_s^{avg} to quantify the variation in hot crack susceptibility.

4. Results and Discussion

The simulations presented below investigate hot cracking tendency during GTAW of the Al-Mg-Si alloy AA6061 for different welding currents and travel speeds. The domain size is ≈2 mm (penetration depth) by ≈3 mm (weld half-width), and ≈1000 μm (along the weld line), and consists of ≈10,000 grains. These values are approximate, since each set of welding parameters will result in a different weld size and grain density. First, the internal and external deformations are presented to investigate their relative contributions to weld mushy zone dynamics. Second, the fluid flow through the mushy zone under differ-

ent welding conditions is examined to gain insight into flow behaviour and the link between flow and microstructure. Then, crack formation in micro liquid channels is predicted and explored.

4.1. Mushy Zone Deformation

A comparison of the average semisolid deformation rates during welding resulting from solidification shrinkage (internal deformation rate) and externally-applied mechanical deformations as calculated by the TMM is shown in Fig. 5. As can be seen, the internal deformation rate is quite high at low solid fraction but decreases as the solidification process advances towards the fully solid state. This a result of the solidification rate $\frac{df_s}{dT}$, which continually decreases with increasing fraction solid for alloys having mostly a primary solid phase such as AA6061. For the problem of hot cracking, fortunately, the low solid fraction at high internal deformation rates enables the healing or liquid refilling of any initiated micro crack. In contrast, the external deformation rate induced by thermomechanical stresses and lateral restraining deformations is seen to be initially small but then becomes quite influential, and will strongly affect hot cracking susceptibility. Further, this term is quite sensitive to welding parameters, whereas the internal deformation rate is not; modifying the welding conditions while still applying a tensile restraining rate of 0.1 s^{-1} (curve 3 to curve 4) is seen to double the average external deformation rate at high solid fraction. Thus, it would appear from these simulations that both welding parameters and restraining strains mainly affect hot cracking susceptibility due to their effect on the semisolid deformations resulting from the thermomechanical response of the base metal.

4.2. Fluid Flow

Fig. 6 compares the FFM results for two different welding conditions at f_s = 0.85. The images on the left show the cross-sectional distribution of the magnitude of the fluid velocity vectors, i.e. $\|\vec{v}_\ell\|$, while the images on the right show the corresponding semisolid microstructure. The semisolid weld shown in

Fig. 6(a) corresponds to a weld fabricated on a clamped plate using a welding current of 140 A and a welding speed of 5 mm s^{-1}. As shown in prior experiments [29], GTAW of a 3 mm sheet of AA6061 under these conditions create in microstructure having an average columnar zone length of 140 μm, and an equiaxed grain size of 68 μm. The figure reveals that fluid flow is not uniform across the cross-section of the weld, but rather experiences severe localization near the centre. This is a result of the localization of deformation within the weld mushy zone. The TMM, Figure 6 of [30], has shown that the micro liquid channels located near the centre of the weld experience much higher deformation rates. This will induce higher fluid velocities in this region, to compensate for the faster separation rates of the channel walls. The semisolid geometry shown in Fig. 6(b) represents the same welding parameters at Fig. 6(a) but because weld microstructure manipulation [29] is assumed, the columnar grains are much longer, at 800 μm but the equiaxed grain size remains the same.. Now, the fluid flow has localized to within the columnar region of the weld. This is because the WSM predicts that the liquid films separating the columnar and equiaxed regions scale with the length of the columnar zone; wider liquid films will transfer higher volumes of molten metal towards the columnar grains thus increasing the volumetric feeding rate.

Fig. 7 plots the average fluid velocity as a function of average f_s across the cross-section of the weld mushy zone for three different externally-applied tensile strain rates. Examining first the data points[2] without external deformation, it can be seen that the fluid velocity decreases significantly with increasing f_s. At very high f_s, the micro liquid channels are quite small, making the permeability of the mush too low to allow for significant fluid flow. Further, the no-flow condition at $f_s = 1$ applies a force acting in the opposite direction, inducing fluid deceleration. The application of external lateral tensile strain raises the fluid velocity throughout the weld mushy zone. These external deformations

[2]Please note that the curves on Fig. 7, as well as Fig. 9, and 11 represent trend lines; the data points come from the simulations

increase the micro liquid channel deformation rates $\dot{\delta}^{i}_{z,ext}$. Consequently, faster flows are needed to compensate for the semisolid deformation. Fig. 8 illustrates the corresponding cross-sectional distribution of the absolute pressure within the semisolid weld at four locations between the weld pool and the fully solidified weld. The solid grains are shaded with the corresponding pressure value of their neighbour channels. As can be seen in the figure, the pressure field is not uniform throughout the micro liquid channel network; the channels near the centre have lowest pressure values. It should be noted that since the arc pressure (boundary condition) was assumed to be 3 atm, the entire set of of micro liquid channels shows a significant pressure drop, approaching nearly 2.8 atm of pressure loss in some regions of the mushy zone. According to Darcy's law, two major factors affect the pressure drop within a porous medium: 1) the velocity of the fluid flowing through the medium, and 2) the permeability of the porous medium, with pressure drop being directly proportional to velocity but inversely proportional to permeability. Therefore, one can conclude that that the higher fluid velocities seen at the centre of the weld in Fig. 6 lead to the localization of pressure drop in this region.

Fig. 9(a) plots the average pressure as a function of average f_s across the cross-section of the weld mushy zone for six different sets of welding parameters, each clamped to a base plate. The figure's legend indicates the welding conditions; the numbers following the V represent the welding speed (mm s^{-1}), while the numbers following I show the welding current (A). In all cases, the average pressure is seen to initially decrease to a minimum value near an average f_s of 0.8 and then rise again close to the final solidification. The initial pressure drop along the weld mushy zone can be linked to the variation in permeability. For a semisolid structure, the permeability is strongly influenced by the micro liquid channel widths; wider channels at lower f_s have higher permeability [6, 20]. Therefore, as the average f_s behind the weld pool increases from 0 to 0.8, the permeability of the weld mushy zone decreases and thus the average pressure drop must increase in order to maintain a relatively fast fluid flow in that region. Interestingly, the increase in the pressure drop does not extend into the

regions with high f_s. This observation is quite different than results for granular solidification models applied to casting, where the pressure drop continues to increase until final solidification. One possible explanation is that at high f_s the external deformation rates applied to the micro liquid channels are smaller since most of the solid network has percolated. At f_s nearing 0.8, there are many micro liquid channels in each lateral bar, each deforming and thus requiring a pressure drop to achieve sufficient fluid flow. By comparing the different sets of data points in Fig. 9(a), it can be seen that welding parameters also affect the average pressure variation with increasing f_s. The model indicates that a weld fabricated by a welding speed of 2 mm s^{-1} and a welding current of 95 A has the smallest minimum average pressure value inside the weld mushy zone, corresponding to the largest pressure drop. This prediction can be explained through the microstructure of the weld where V2I95 has a long columnar zone [29]. As demonstrated through Fig. 6, larger columnar grains intensify the fluid velocity through the columnar zone, correspondingly requiring larger pressure drops.

Fig. 9(b) shows the effect of welding constraints on the average pressure along the weld mushy zone for four different external lateral tensile strain rates. The weld was fabricated at a welding current of 120A and a welding speed of 4 mm/s. Based on the obtained results, increasing the external strain rate from 0 to 0.1 s^{-1} slightly amplifies the pressure drop inside the weld mushy zone. The pressure drop decreases significantly at larger external strains, as shown by the data points for 1 s^{-1}. This phenomenon can be linked to the effects of welding constraints on the fluid velocity field. As depicted in Fig. 7, increasing the external lateral tensile strain rate to even 0.1 s^{-1} significantly raises the average fluid velocity through the weld mushy zone, inducing larger pressure drops. For a clamped weld, the results of the model show that the pressure drop between the weld pool and high average f_s regions at the end of the weld mushy zone is nearly 2 atm (Fig. 9(a)). This result is fairly similar to the pressure drop calculated by Coniglio and Cross during GTAW of clamped aluminum plates [31]. Using the RDG model, they have reported that the pressure drop between the aluminum weld pool and the end of the mushy zone

with $f_s = 0.98$ varies in the range of 0.11 and 0.55 atm. Multi-physics models of hot cracking provide much more detailed information as compared to the RDG criterion, however, such as the occurrence and location of defects as explored below.

4.3. Defect Formation

The CIM detects defected micro liquid channels within a semisolid RVE. Fig. 10 shows qualitatively the location of defected micro liquid channels as a function of average f_s. These RVEs can be interpreted as either the various states of a specific location within a weld at different times during the welding process or at different sections along the weld mushy zone as shown in Fig. 3. Note that the defected channels formed at one average f_s are not transferred to the next in order to obtain a better understanding regarding the role of the mushy zone structure on defect localization. As can be seen, the defected channels formed at low average f_s are mainly located inside the columnar zone where the fluid experiences high deformation rates [30]. Upon approaching the fully solidified end of the weld mushy zone, however, the fluid velocity within each channel decreases significantly (Fig. 7 while the external deformation rate increases significantly. This causes a noticeable jump in the number of defected channels, which are mostly located within the equiaxed region and near the weld centreline. Such a shift from the columnar zone to the centre of the weld can be linked to the fact that with increasing f_s, the mushy zone deformation localizes to the centre of the weld since it is the last region to solidify.

To quantify the occurrence of channel defects that would initiate a hot crack, a $Kou\ Crack\ Index$ is defined and given by the percentage of total micro liquid channels having $KCC > 0$ at a given f_s. Hence, the defect index only accounts for the newly defected channels and not the defects formed at a previous f_s. Note also that RVEs with f_s smaller than 0.7 are not considered since it was assumed that there is sufficient fluid flow to heal any newly-formed hot crack in these areas of the mushy zone. Fig. 11(a) shows the Kou crack index for six welds fabricated under an external lateral tensile strain rate of 0.1 s^{01} with

different welding parameters. A number of salient observations can be made. First, the areas with higher average f_s are, relatively, very susceptible to hot cracking as zones closer to the weld pool show negligible defected micro liquid channels and thus have negligible contribution to the formation of hot cracks. As discussed in Section 2.4, the Kou cracking criterion indicates that a conjunction of fast deformation rates (the first term on the r.h.s. of Eq. 10 and slow slow fluid flow (the third term on the r.h.s. of Eq. 10 induce hot tearing. As seen in Fig. 10, the relatively fast fluid flow within the RVEs occurring at low average f_s can accommodate for the deformation of the semisolid structure and hence limits the occurrence of hot cracking to a few channels. Second, the role of welding parameters on hot cracking, and specifically the travel speed, is revealed by comparing the six provided sets of data points. As can be seen, the model results reproduce the well-known behavior whereby increased travel speed lowers the susceptibility of the weld mushy zone to hot tearing. Analysis of the model results reveals the mechanism resulting in this phenomenon. Specifically, a higher travel speed increases the cooling rate, which lowers the number of unbridged channels capable of developing defects at high average f_s where the accumulated deformation and slow fluid velocity can cause hot cracking. Fig. 11(b) examines the effect of external lateral tensile strain rates on the *Kou Crack Index*. As can be seen, increasing the external strain rate, especially above a value of 0.1 s^{-1} significantly increases this index to a point where more than one percent of all the micro liquid channels have cracked. Thus, this value could be used as the critical strain rate for the formation of hot cracks during GTAW of AA6061. The observed correlation between the externally-applied strain rate and the formation of hot cracks is a result of the fact that as shown by the TMM the external strain rate will increase $\dot{\delta}^i_{z,ext}$ for each micro liquid channel, making the weld mushy zone more susceptible to hot cracking.

4.4. Model Verification

The results of the proposed multi-physics welding model are quite close to the outcomes of several experimental studies. In terms of hot cracking, Arata

et al. [33] reported a critical strain rate value of 0.25 s^{-1} in arc welding of Al-Mg-Si alloys, while Coniglio and Cross reported a critical external strain rate value during GTAW of Al alloys of between 0.05 and 0.3 s^{-1} [31]. Both values are quite similar to the value of 0.1 s^{-1} obtained in this study. In terms of welding travel speed, Matsuda et al. have reported that, in Al alloys, increasing the travel speed from 2.5 mm s^{-1} to 13 mm s^{-1} during GTAW can improve the hot cracking resistance [34]. Chihoski [35] showed that at high welding travel speeds, a compressive stress field forms near the mushy zone, preventing hot cracking. Niel et al. [10] showed that for a constant current in GTAW, increasing the welding travel speed can prevent hot cracking in AA 6061 aluminum alloys. These findings are consistent with the finding of the present model. Prior welding experiments have also shown that reducing the size of the columnar zone through grain size manipulation techniques will reduce hot cracking, qualitatively matching the results shown in Fig 6. In separate studies, Mousavi et al. [36], Warrington et al. [37], and Dvornak et al. [38] each demonstrated that a reduction in Al alloy hot crack susceptibility could be achieved through the addition of grain refiners that shorten the columnar region inside the weld. Also, a recent synchrotron radiography experimental study on initiation and growth kinetics of solidification cracking during welding by Aucott et al. [39] confirms several hot cracking features predicted by the present model. Specifically, hot cracking is mainly driven by the strain acting on the solidifying weld, and further, micro cracks first initiate inside the columnar region near the fusion boundary and at later stages of solidification they begin to form at the core of the weld. This fracture growth pattern is quite similar to the crack advancement predicted by the model in Fig. 10 where hot cracks first initiate near the fusion boundary but the migrate towards the center of the weld as the average f_s increases.

5. Conclusions

A 3D multi-scale multi-physics model of GTAW has been developed to predict hot crack formation in aluminum alloys. The model is made up of four modules: (I) a welding solidification module, (II) a thermo-mechanical analysis module, (III) a fluid flow module, and (IV) a crack initiation module. The model considers the effects of solidification contraction, the response of the base metal during welding, the application of external deformation, and fluid flow throughout the mushy zone on hot cracking susceptibility. With this information, the localization of hot cracks at individual grain boundaries as well as the overall hot cracking susceptibility are predicted. The model was verified against prior numerical and experimental data available in the literature, and qualitatively agree with these prior results.

Analysis of the simulations results help to explain the metallurgical mechanisms underlying hot crack occurrence during GTAW. First, the welding current and travel speed affect hot tearing susceptibility by strongly influencing the deformation rates of the micro liquid channels, and the number of unbridged liquid channels capable of developing defects. Second, microstructure manipulation methods that lengthen the columnar zone increases the volumetric feeding rate. Third, the non-uniform liquid flow within the weld mushy zone that results from complex microstructure creates regions of very low pressure that act as crack nucleation sites. When the mushy zone cannot be fed, a hot crack will occur. Interestingly, micro cracks were predicted to initiate near the fusion zone but then localize at the core of the weld.

Acknowledgements

The authors wish to thank the American Welding Society (AWS), Rio Tinto Alcan, and the Natural Sciences and Engineering Research Council of Canada (NSERC) for financial support.

6. Data Availabilitydd

The raw/processed data required to reproduce these findings cannot be shared at this time due to its size, but representative sample data is included in the Figures.

References

[1] S. Kou, A criterion for cracking during solidification, Acta Materialia 88 (2015) 366–374.

[2] S. Kou, Welding Metallurgy, John Wiley and Sons Inc, Hoboken, New Jersey, 2003.

[3] N. R. Mandal, Welding defects, Ship Construction and Welding (2017) 283–292.

[4] T. Boellinghaus, J. C. Lippold, C. E. Cross, Cracking Phenomena in Welds IV, Springer, 2016.

[5] Y. Feng, P. Mao, Z. Liu, Z. Wang, J. Qin, F. Wang, Hot tearing susceptibility of mgzn4.5, China Foundry 13 (3) (2016) 159–165.

[6] M. Sistaninia, A. B. Phillion, J. M. Drezet, M. Rappaz, Three-dimensional granular model of semi-solid metallic alloys undergoing solidification: Fluid flow and localization of feeding, Acta Materialia 60 (9) (2012) 3902–3911.

[7] J. C. Lippold, Recent developments in weldability testing, in: Hot Cracking Phenomena in Welds, 2005, pp. 271–290.

[8] J. C. M. Farrar, Hot cracking tests-the route to international standardization, in: Hot Cracking Phenomena in Welds, 2005, pp. 291–305.

[9] M. A. Jaafar, D. R. Rousse, S. Gibout, J. P. Bédécarrats, A review of dendritic growth during solidification: Mathematical modeling and numerical simulations, Renewable and Sustainable Energy Reviews 74 (2017) 1064–1079.

[10] A. Niel, F. Deschaux-Beaume, C. Bordreuil, G. Fras, J. M. Drezet, Hot tearing test for tig welding of aluminum alloys: Application of a stress parallel to the fusion line, in: Hot cracking phenomena in welds III, 2011, pp. 43–59.

[11] A. B. Phillion, Recent experimental and numerical developments in semisolid deformation, JOM 66 (8) (2014) 1406–1407.

[12] M. Sistaninia, S. Terzi, A. B. Phillion, J. M. Drezet, M. Rappaz, 3-d granular modeling and in situ x-ray tomographic imaging: a comparative study of hot tearing formation and semi-solid deformation in al-cu alloys, Acta Materialia 61 (10) (2013) 3831–3841.

[13] Z. Sun, M. Bernacki, R. Logé, G. Gu, Numerical simulation of mechanical deformation of semi-solid material using a level-set based finite element method, Modelling and Simulation in Materials Science and Engineering 25 (6) (2017) 065020.

[14] S. A. Khairallah, A. T. Anderson, A. Rubenchik, W. E. King, Laser powder-bed fusion additive manufacturing: Physics of complex melt flow and formation mechanisms of pores, spatter, and denudation zones, Acta Materialia 108 (2016) 36–45.

[15] W. Yan, W. Ge, Y. Qian, S. Lin, B. Zhou, W. K. Liu, G. J. Wagner, Multi-physics modeling of single/multiple-track defect mechanisms in electron beam selective melting, Acta Materialia 134 (2017) 324–333.

[16] A. B. Phillion, S. L. Cockcroft, P. D. Lee, A three-phase simulation of the effect of microstructural features on semi-solid tensile deformation, Acta Materialia 56 (16) (2008) 4328–4338.

[17] A. B. Phillion, J. L. Desbiolles, M. Rappaz, A 3d granular model of equiaxed-granular solidification, in: Modeling of Casting Welding and Advanced Solidification Processes XII, TMS, 2009, pp. 353–360.

[18] M. Sistaninia, A. B. Phillion, J. M. Drezet, M. Rappaz, Simulation of semi-solid material mechanical behavior using a combined discrete/finite element method, Metallurgical and Materials Transactions A 42 (1) (2011) 239–248.

[19] M. Sistaninia, A. B. Phillion, J. M. Drezet, M. Rappaz, A 3-d coupled hydromechanical granular model for simulating the constitutive behavior of metallic alloys during solidification, Acta Materialia 60 (19) (2012) 6793–6803.

[20] S. Vernede, P. Jarry, M. Rappaz, A granular model of equiaxed mushy zones: Formation of a coherent solid and localization of feeding, Acta Materialia 54 (15) (2006) 4023–4034.

[21] S. Vernède, M. Rappaz, A simple and efficient model for mesoscale solidification simulation of globular grain structures, Acta materialia 55 (5) (2007) 1703–1710.

[22] J. F. Zaragoci, L. Silva, M. Bellet, C. A. Gandin, Numerical tensile test on a mushy zone sample, in: Materials Science and Engineering 33, IOP Conference Series, 2012, p. 012054.

[23] V. Mathier, A. Jacot, M. Rappaz, Coalescence of equiaxed grains during solidification, Modelling and simulation in materials science and engineering 12 (3) (2004) 479–490.

[24] W. Dijkstra, C. Vuik, A. Dammers, K. L., Network modeling of liquid metal transport in solidifying aluminum alloys, in: M. Rappaz, C. Beckermann, R. Trivedi (Eds.), Solidification Processes and Microstructures, TMS, 2004, pp. 151–156.

[25] D. Lahaie, M. Bouchard, Physical modeling of the deformation mechanisms of semisolid bodies and a mechanical criterion for hot tearing, Metallurgical and Materials Transactions A 32 (697-705).

[26] J. Liu, Z. Rao, S. Liao, Modeling of transport phenomena and solidification cracking in laser spot bead-on-plate welding of aa6063-t6 alloy. part i—

the mathematical model, International Journal of Advanced Manufacturing Technologies 73 (2014) 1705–1716.

[27] J. Sengupta, S. Cockcroft, D. Maijer, A. Larouche, Quantification of temperature, stress, and strain fields during the start-up phase of direct chill casting process by using a 3d fully coupled thermal and stress model for aa5182 ingots., Materials Science and Engineering A (2005) 157–177.

[28] V. Ploshikhin, A. Prikhodovsky, M. Makhutin, A. Ilin, H.-W. Zoch, Integrated mechanical-metallurgical approach to modeling of solidification cracking in welds, in: Hot Cracking Phenomena in Welds, 2005, pp. 223–244.

[29] H. Z. Rajani, A. B. Phillion, A mesoscale solidification simulation of fusion welding in aluminum-magnesium-silicon alloys, Acta Materialia 77 (2014) 162–172.

[30] H. Z. Rajani, A. B. Phillion, 3-d multi-scale modeling of deformation within the weld mushy zone, Materials and Design 94 (2016) 536–545.

[31] N. Coniglio, C. E. Cross, T. Michael, M. Lammers, Defining a critical weld dilution to avoid solidification cracking in aluminum, Welding Journal 87 (2008) 237–247.

[32] S. W. Campbell, A. M. Galloway, N. A. McPherson, Arc pressure and weld metal fluid flow while using alternating shielding gases. part 1: arc pressure measurement, Science and Technology of Welding and Joining 18 (7) (2013) 591–596.

[33] Y. Arata, F. Matsuda, K. Nakata, K. Shinozaki, Solidification crack susceptibility of aluminum alloy weld metals (report ii)-effect of straining rate on cracking threshold in weld metal during solidification, Transactions of JWRI 6 (1) (1977) 91–104.

[34] F. Matsuda, H. Nakagawa, K. Nakata, H. Okada, The vdr cracking test for solidification crack susceptibility on weld metals and its application to aluminum alloys, Transactions of JWRI 8 (1979) 85–95.

[35] R. A. Chihoski, Expansion and stress around aluminum weld puddles, Welding Journal 58 (9) (1979) 263–276.

[36] M. G. Mousavi, C. E. Cross, O. Grong, Effect of scandium and titanium-boron on grain refinement and hot cracking of aluminum alloy 7108, Science and Technology of Welding and Joining 4 (6) (1999) 381–388.

[37] D. Warrington, D. G. McCartney, Development of a new hot cracking test for aluminum alloys, Cast Metals 2 (3) (1989) 134–143.

[38] M. J. Dvornak, R. H. Frost, D. L. Olson, The weldability and grain refinement of al-2. 2 li-2. 7 cu, Welding Journal 68 (1989) 327–337.

[39] L. Aucott, D. Huang, H. B. Dong, S. W. Wen, J. A. Marsden, A. Rack, A. C. F. Cocks, Initiation and growth kinetics of solidification cracking during welding of steel, Scientific Reports 7 (2017) 40255.

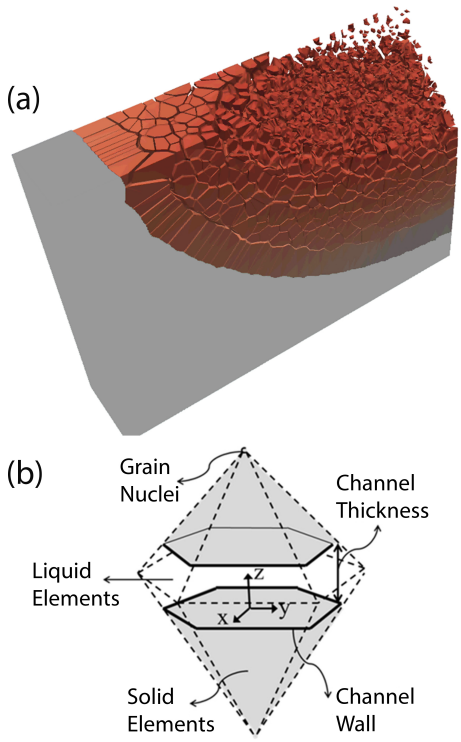

Figure 1: (a): Welding semisolid microstructure predicted by the WSM for GTAW of a 3 mm AA60601 sheet using a welding current of 140 A and a travel speed of 5 mm/s. (b) Schematic showing the elementary solid and liquid elements.

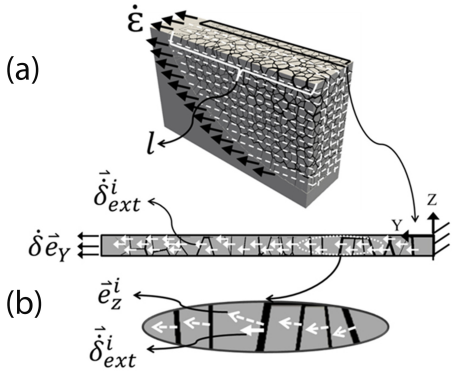

Figure 2: (a): Discretization of the welding mushy zone into lateral bar elements. Each bar element is indicated by dotted white lines, while the black arrows indicate the lateral deformation applied by the base material. (b) Schematic depicting the decomposition of the global deformation rate into external normal deformation rate vectors. After [30].

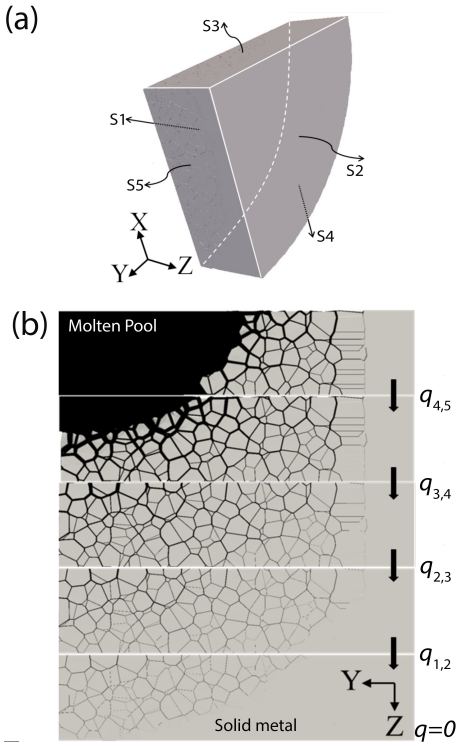

Figure 3: (a) Boundary conditions applied to the FFM RVE. (b) Schematic illustrating the mushy zone segments used to sequentially compute fluid flow within the weld mushy zone; the term q denotes the flux transfer from one segment to another.

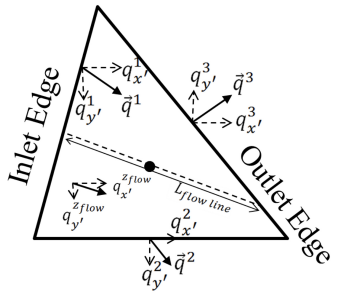

Figure 4: Fluid flux components within a micro liquid channel showing the dominant flow line.

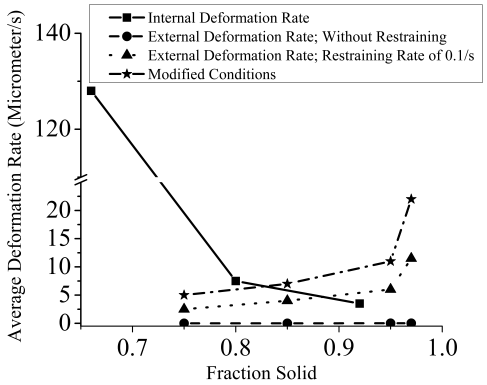

Figure 5: Comparison of the internal deformation rate resulting from the solidification shrinkage, and the external deformation rates for a clamped weld and one where a tensile restraining rate of 0.1 s^{-1} is applied, as calculated by the TMM, for a weld fabricated using a welding current of 140 A and a welding speed of 5 mm s^{-1}. The curve *Modified Conditions* was produced using welding conditions of 95 A, a welding speed of 2 mm s^{-1}, and a tensile restraining rate of 0.1 s^{-1}.

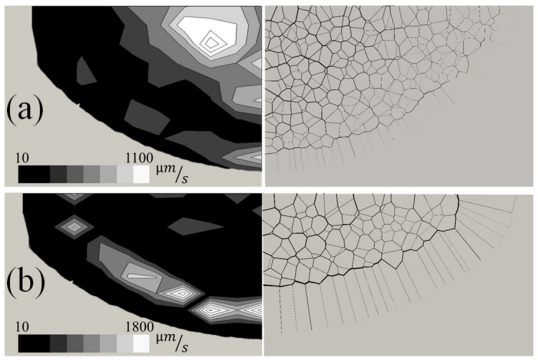

Figure 6: Cross-sectional distribution of the magnitude of the fluid velocity vector at an average f_s of 0.85 for a weld fabricated on a clamped plate using a welding current of 140 A and a welding speed of 5 mm s^{-1}, and having (a) an average columnar zone length of 140 μm; (b) an average columnar zone length of 800 μm. The contours on the left show the distribution of the magnitude of the fluid velocity, while the images on the right show their corresponding microstructure.

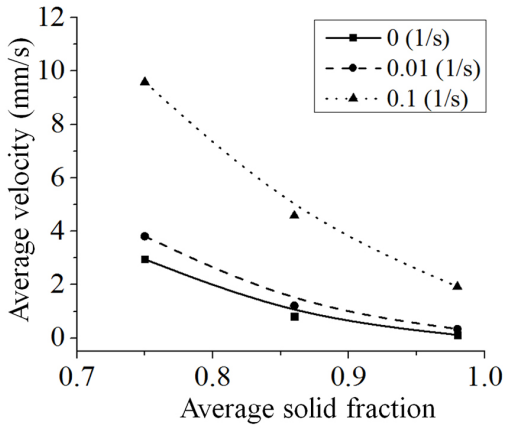

Figure 7: The variation in the average fluid velocity as a function of the average f_s for a weld fabricated for three different external lateral tensile strain rates. The weld was fabricated at a welding current of 140 A and a welding speed of 5 mm/s.

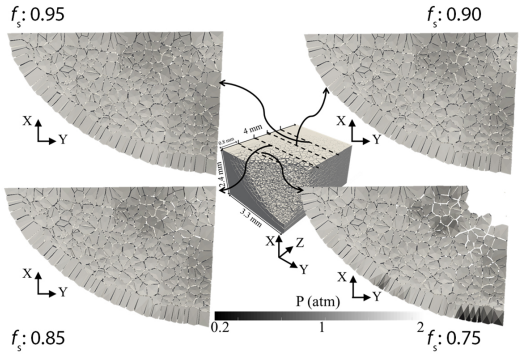

Figure 8: Cross-sectional distribution of the absolute pressure at different average f_s for a semisolid weld fabricated using a welding current of 140 A and a welding speed of 5 mm s^{-1}. All pressures are below the applied arc pressure of 3 atm.

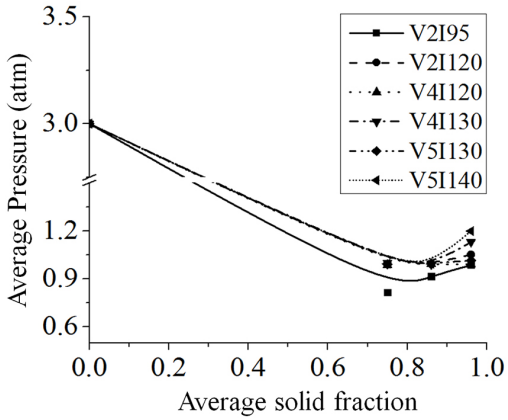

(a)

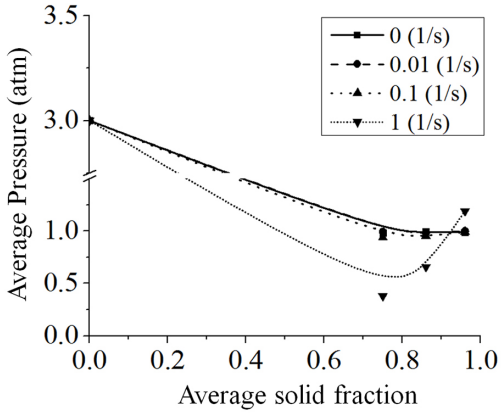

(b)

Figure 9: (a) The variation in average pressure as a function of average f_s for a clamped weld with various welding parameters. (b) The variation in the average pressure along the weld mushy zone for four different external lateral tensile strain rates. The weld was fabricated at a welding current of 120 A and a welding speed of 4 mm s^{-1}.

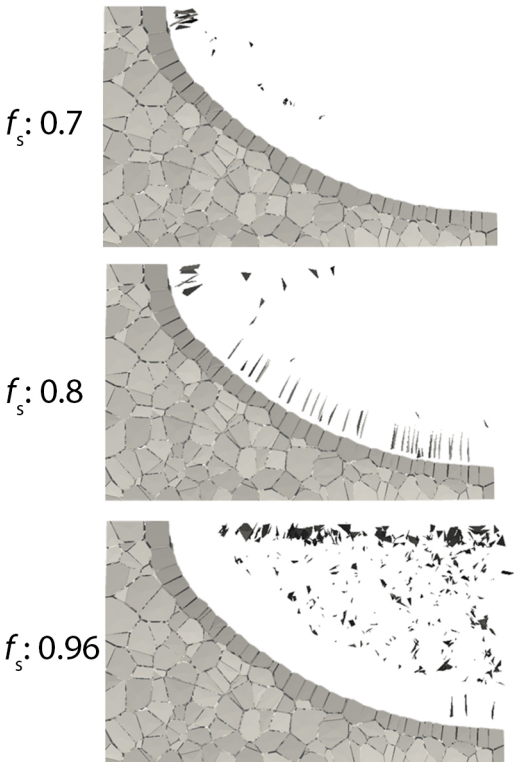

Figure 10: The distribution of newly defected channels at three different average f_s of 0.7, 0.8, and 0.96 based on the Kou cracking criterion. The weld was fabricated at a welding current of 120 A and a welding speed of 4 mm s^{-1}.

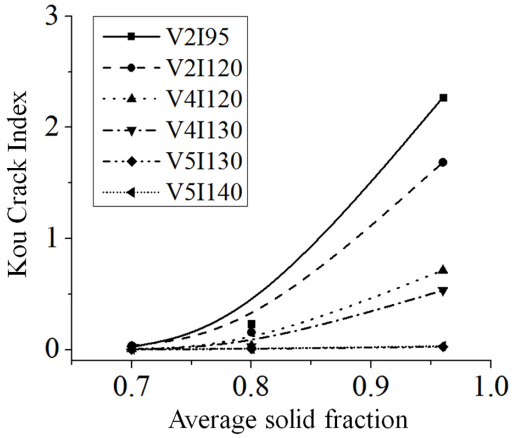

(a)

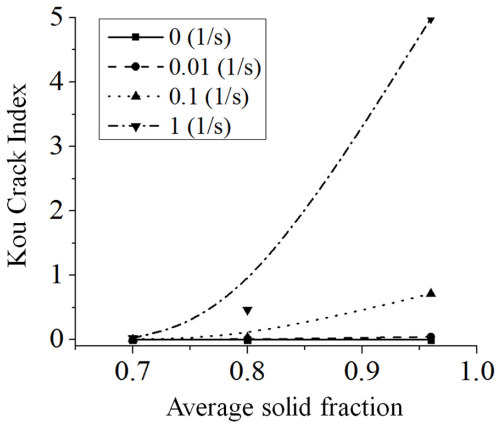

(b)

Figure 11: (a) The Kou crack index for different RVE's with different average f_s along the weld mushy zone. The welds are fabricated on a plate under an external lateral tensile strain rate of 0.1 s^{-1} with six different sets of welding parameters. (b) The variation of the Kou crack index along the mushy zone of a weld fabricated at a welding speed of 4 mm s^{-1} and a welding current of 120 A under various external lateral tensile strain rates.